JGR Space Physics

METHOD
10.1029/2023JA031527

A Ground-Based Instrument Suite for Integrated High-Time Resolution Measurements of Pulsating Aurora With Arase

K. Hosokawa[1], S.-I. Oyama[2,3,4], Y. Ogawa[3], Y. Miyoshi[2], S. Kurita[5], M. Teramoto[6], S. Nozawa[2], T. Kawabata[2], Y. Kawamura[1], Y.-M. Tanaka[3], H. Miyaoka[3], R. Kataoka[3], K. Shiokawa[2], U. Brändström[7], E. Turunen[8], T. Raita[8], M. G. Johnsen[9], C. Hall[9,†], D. Hampton[10], Y. Ebihara[5], Y. Kasahara[11], S. Matsuda[11], I. Shinohara[12], and R. Fujii[13]

[1]Graduate School of Communication Engineering and Informatics, University of Electro- Communications, Tokyo, Japan, [2]Institute for Space-Earth Environmental Research, Nagoya University, Nagoya, Japan, [3]National Institute of Polar Research, Tokyo, Japan, [4]University of Oulu, Oulu, Finland, [5]Research Institute for Sustainable Humanosphere, Kyoto University, Uji, Japan, [6]Kyushu Institute of Technology, Fukuoka, Japan, [7]The Swedish Institute of Space Physics, Kiruna, Sweden, [8]Sodankylä Geophysical Observatory, Sodankylä, Finland, [9]Tromsø Geophysical Observatory, UiT, The Arctic University of Norway, Tromsø, Norway, [10]Geophysical Institute, University of Alaska Fairbanks, Fairbanks, AK, USA, [11]Graduate School of Natural Science and Technology, Kanazawa University, Kanazawa, Japan, [12]Institute of Space and Astronautical Science, Sagamihara, Japan, [13]Research Organization of Information and Systems, Tokyo, Japan

[†]Deceased 9 August 2021.

Key Points:

- An integrated package of instruments for high-time resolution measurements of pulsating aurora was deployed in Scandinavia and Alaska
- The system has enabled us to capture the fine-scale spatio-temporal variations of pulsating aurora in a wide area
- Data from those instruments have also been used for simultaneous observations of pulsating aurora with the Arase satellite

Supporting Information:

Supporting Information may be found in the online version of this article.

Correspondence to:

K. Hosokawa,
keisuke.hosokawa@uec.ac.jp

Citation:

Hosokawa, K., Oyama, S.-I., Ogawa, Y., Miyoshi, Y., Kurita, S., Teramoto, M., et al. (2023). A ground-based instrument suite for integrated high-time resolution measurements of pulsating aurora with Arase. *Journal of Geophysical Research: Space Physics*, *128*, e2023JA031527. https://doi.org/10.1029/2023JA031527

Received 12 APR 2023
Accepted 2 JUL 2023

Author Contributions:

Project Administration: C. Hall
Resources: C. Hall
Supervision: C. Hall

Abstract A specialized ground-based system has been developed for simultaneous observations of pulsating aurora (PsA) and related magnetospheric phenomena with the Arase satellite. The instrument suite is composed of (a) six 100 Hz sampling high-speed all-sky imagers (ASIs), (b) two 10 Hz sampling monochromatic ASIs observing 427.8 and 844.6 nm auroral emissions, (c) a 20 Hz sampling fluxgate magnetometer. The 100 Hz ASIs were deployed in four stations in Scandinavia and two stations in Alaska, which have been used for capturing the main pulsations and quasi 3 Hz internal modulations of PsA at the same time. The 10 Hz sampling monochromatic ASIs have been operative in Tromsø, Norway with the 20 Hz sampling magnetometer. Combination of these multiple instruments with the European Incoherent SCATter (EISCAT) radar enables us to detect the low-altitude ionization due to energetic electron precipitation during PsA and further to reveal the ionospheric electrodynamics behind PsA. Since the launch of the Arase satellite, the data from these instruments have been examined in comparison with the wave and particle data from the satellite in the magnetosphere. In the future, the system can be utilized not only for studies of PsA but also for other classes of aurora in close collaboration with the planned EISCAT_3D project.

1. Introduction

Pulsating aurora (PsA) is a common auroral phenomenon often observed during the recovery phase of auroral substorms (see recent reviews by Lessard, 2012; Hosokawa et al., 2015; Nishimura et al., 2020). PsA is produced by intermittent precipitations of a few to a few tens of keV electrons caused by the pitch angle scattering in the magnetosphere (Miyoshi et al., 2010, 2015a; Nishiyama et al., 2011). Chorus and Electron Cyclotron Harmonic (ECH) waves have been considered as agents driving this wave-particle interaction process (Fukizawa et al., 2018; Nishimura et al., 2010). Recent magnetospheric observations by the Arase satellite (Miyoshi, Shinohara, et al., 2018) demonstrated that chorus waves actually cause PsA through scattering of energetic electrons into the loss cone (S. Kasahara et al., 2018) and determine the temporal variations of PsA (Hosokawa et al., 2020; Ozaki et al., 2019).

One of the unique characteristics of PsA, that are different from other types of auroras, is its complicated temporal variations. The temporal variation of PsA is known to consist of two distinct periodicities. One is the "main pulsation" in the timescale from a few to a few tens of seconds which is observed for almost all the cases of PsA (e.g., Yamamoto, 1988). The other is much faster modulations, which are often called "internal modulations" or "quasi 3 Hz modulations." These sub-second variations are embedded within the ON phase of the main pulsation (Sandahl et al., 1980). The internal modulations are observed in many cases of PsA, but their appearance is known to depend on MLT (Røyrvik and Davis, 1977).

Miyoshi, Saito, et al. (2015) proposed a model explaining the origins of two periodicities of PsA (i.e., main pulsation and internal modulations) considering the characteristics of wave-particle interactions with chorus.

They suggested that repetitive bursts of chorus (chorus bursts), which appear every a few seconds, cause the main pulsation of PsA, while rising tone chorus elements embedded in a chorus burst produce flux variations of electron precipitation responsible for the internal modulations (Demekhov & Trakhtengerts, 1994; Foster & Rosenberg, 1976; Rosenberg et al., 1971). Recently, this model has been successfully tested by simultaneous conjugate observations of PsA from the ground and chorus waves by the Arase satellite in the magnetosphere (e.g., S. Kasahara et al., 2018; Hosokawa et al., 2020).

High-time resolution optical observations in the last decade discovered further faster modulations whose frequency is higher than 10 Hz. For example, Samara and Michell (2010) identified 12 Hz modulations in the time-series of PsA. Kataoka et al. (2012) showed ∼54 Hz modulations in data from a high-speed camera. Although there have been a few reports about these fast modulations, it still remains an open question what processes produce such faster modulations beyond 10 Hz. One of the possible origins of these faster modulations is the so-called "subpacket" structure embedded within a single element of chorus (Foster et al., 2017). The subpacket structure is considered to be formed by repetitive saturations of nonlinear wave growth (e.g., Omura et al., 2019), which could be a key process for characterizing the temporal evolution of chorus waves.

THEMIS-GBO (Time History of Events and Macroscale Interactions during Substorms—Ground-Based Observatory) successfully observed the dynamics of aurora including PsA in a wide area in North America (Mende et al., 2008). However, the temporal resolution of the ASIs of THEMIS-GBO, that is, 3 s, was not always sufficient to observe both the main pulsation and internal modulation of PsA; thus, it has still been difficult to reveal the full spectrum of PsA periodicity in a wide area. To overcome this bottle neck, we have developed an instrument package for observations of PsA, which can be a high-time resolution version of THEMIS-GBO although the coverage is relatively limited as compared to THEMIS-GBO at this stage. As summarized in the earlier part of this section, there are three distinct periodicities in the time-series of PsA: (a) main pulsation (a few to a few tens of second), (b) internal modulations (∼3 Hz), and (c) faster modulation (>10 Hz). In order to detect all of these variations, it is needed to install high-time resolution ASIs, whose temporal resolution is, for example, 100 Hz.

It has also been known that PsA has a broad impact on the ionosphere and middle atmosphere (Miyoshi et al., 2021; Oyama et al., 2017; Turunen et al., 2016). In this sense, in addition to the wide coverage of the optical observations, it is also demanded to conduct integrated and comprehensive observations by combining ground-based radio and optical observations. For this purpose, we deployed two monochromatic ASIs and a high-time resolution ground-based magnetometer in Tromsø, Norway where the EISCAT radar is operative. Data from the monochromatic ASIs can be used to estimate the characteristics energy of precipitating electrons following methods introduced, for instance, by Ono (1993) and Lanchester et al. (1994).

In this report, we introduce the technical detail of the instruments as a combined suite for observing PsA in close comparison with magnetospheric satellite and ground-based radars. In addition, we show how data from these instruments have been used for studies of PsA in combination with observations of the Arase satellite and the EISCAT radar. Especially, by showing several case examples, we demonstrate a combination of (a) clustering of high-speed ASIs in wide areas, and (b) multi-instrumental observation at one specific site (i.e., Tromsø) is helpful for understanding the spatial distribution of the two periodicities of PsA and the electrodynamics existing behind low-altitude ionization during intervals of PsA.

2. Instruments

2.1. 100 Hz All-Sky Imagers

The 100 Hz all-sky imager (ASI) is composed of an EMCCD (Electron Multiplying Charge-Coupled Device) camera of Hamamatsu Photonics (C9100-23B) and C-mount fish-eye lens of Fujinon Co. Ltd (FE185C086HA-1). The EMCCD camera has an imaging part whose resolution is 512×512 pixels. Before sending out from the camera, however, the images are binned with 2×2 windows and the spatial resolution of the final output images turns out to be 256×256 pixels. The images are transferred from the camera to the Personal Computer (PC) by using a camera control software and saved to the internal solid state drive (SSD). When the images are saved to data files, 6,000 images obtained during a 1 min interval are compiled and stored in a single "raw format" file with 16-bit depth. The typical raw count for the 100 Hz ASI observations is a few thousands with the amplification factor of ∼100.

Figure 1 shows a block diagram of the entire system of the 100 Hz sampling ASI. The camera is externally triggered by a combination of the USB signal generator (USB-SG trigger unit) and GNSS-based 1PPS pulse

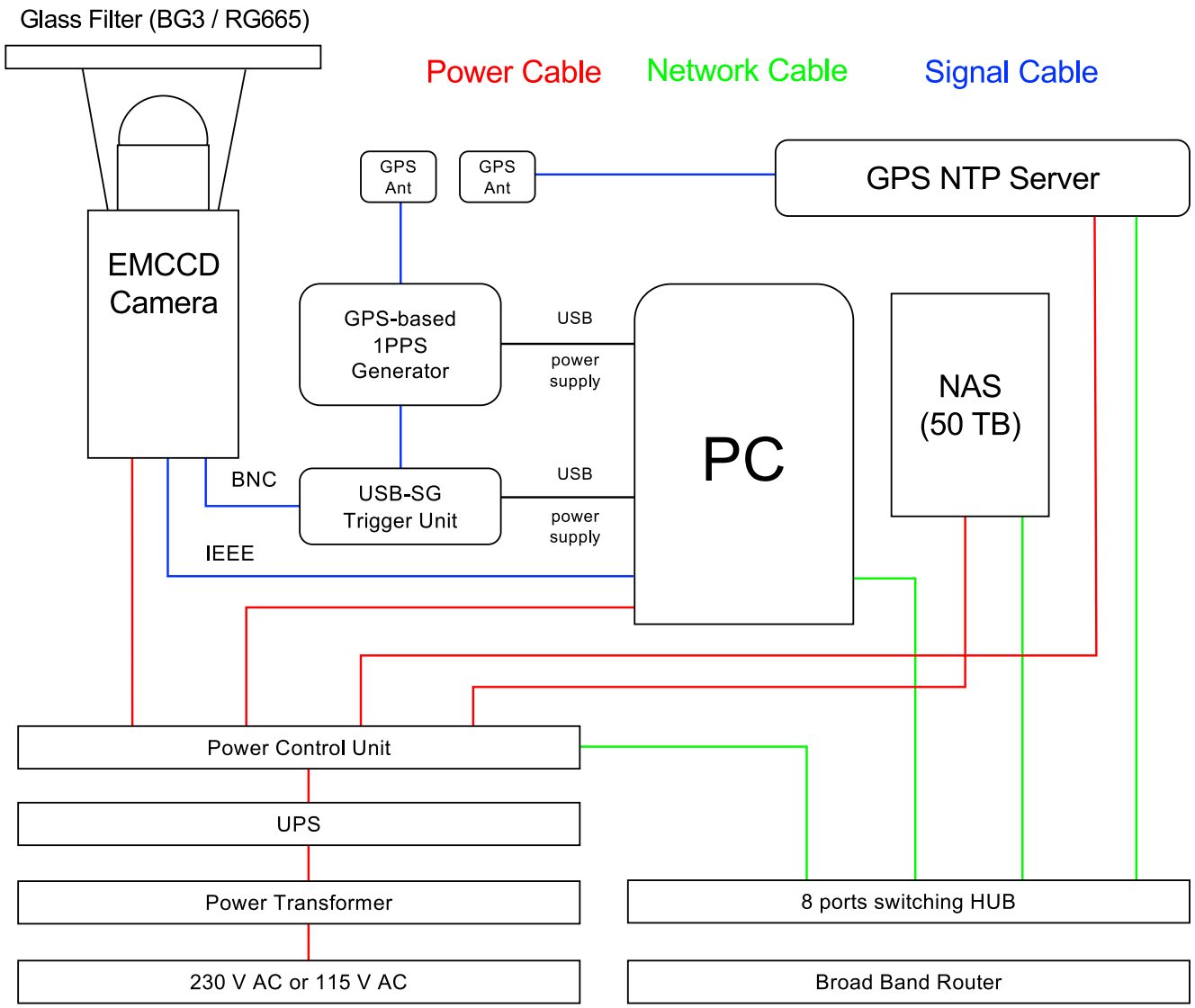

Figure 1. Block diagram of the 100 Hz ASI system.

generator. The USB-SG trigger unit (AWG-10K of ELMOS Co.,Ltd.) is configured to produce a 1 s length single sequence pulse train containing 100 square pulses responding an external trigger provided every 1 s. These square pulses are input to the EMCCD camera and keep the camera taking 100 images per second. The USB-SG trigger unit is further triggered every 1 s by the GNSS-based 1PPS pulse generator (VN-870 of Furuno Co.,Ltd) which is based on a multi-GNSS receiver module (GT-87 of Furuno Co.,Ltd). VN-870/GT-87 receives navigation signals from GPS, GLONASS, QZSS, SBAS allowing it to output accurate and robust 1PPS synchronized to UTC time. The combination of the USB-SG and the GNSS-based 1PPS pulse generator is able to trigger the EMCCD camera 100 times per second and the timings of the triggering is synchronized to UTC time, which allows us to compare the sub-second resolution all-sky images obtained by multiple EMCCD ASIs distributed in a wide area. The camera is directly connected to the PC with an IEEE1394 cable, and the images can be captured and saved without significant image losses. On average, image loss happens approximately once every 100,000 samplings. The maximum frame rate for retrieving images from the camera is ~137 Hz for the case of 2 × 2 binning, which is a hardware limit. We have tested the observation with this maximum frame rate of ~137 Hz, but the occurrence rate of frame loss was slightly higher during the image transfer from the camera; thus, we have been operating the camera with the slightly reduced frame rate at 100 Hz. We use the internal SSD drive rather than hard drive (HDD) as a device for saving images because the use of HDD introduced much more frequent image loss due to

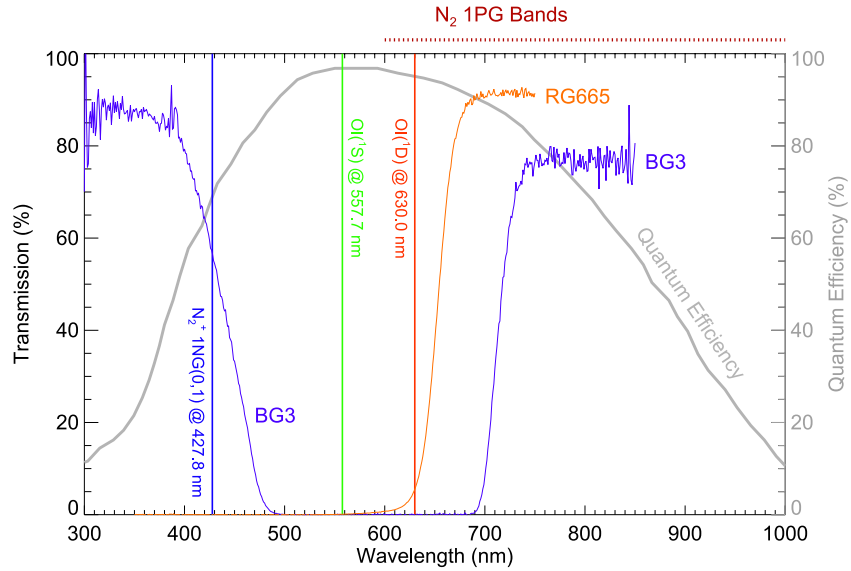

Figure 2. Transmission characteristics of the RG665 (orange) and BG3 (purple) glass filters used for the 100 Hz ASI observations. The quantum efficiency of the EMCCD camera is also shown. Several auroral emission lines are overplotted for comparison.

the slower data writing speed. We automatically run the camera from the beginning of astronomical twilight in the evening to the end of astronomical twilight in the next morning (when the Sun is below the horizon by −12°) independent of the Moon phase.

The clock of the PC is adjusted every minute using the GNSS NTP server prepared within the local private network. The accuracy of the clock of the PC is as large as a few msec which is less than the sampling interval of the ASI. The size of the raw data for a 1-min interval is ∼750 MB. The raw data files are stored in the local SSD drive, whose size is 1 TB, during the nighttime observation, and then copied to the external NAS storage during the daytime. The observations in the winter season normally start at the beginning of September and finish in the end of March. During the operational period, due to the limitation of the onsite NAS storage, we only keep good data obtained when the local weather condition is good and aurora activity is identified, by checking the quick look data (keograms and movies) at https://ergsc.isee.nagoya-u.ac.jp/psa-gnd/bin/psa.cgi.

To capture the rapid temporal variation of PsA, especially sub-second internal modulations, it is needed to cut out the slower auroral emission lines. For example, the emission at 557.7 nm is known to have a systematic delay due to the finite lifetime of O(^{1}S) excited state of oxygen atom (∼0.7 s) and that at 630.0 nm is known to show much longer delay of ∼110 s again due to the lifetime of O(^{1}D) state (e.g., Jones, 1974). Unless we do remove the contribution of these slower emissions, it is difficult to associate the rapid modulation of PsA, such as internal modulations and further faster ones, with fine-scale temporal variations in chorus waves at the magnetospheric counterpart. For this reason, we considered to use wideband optical filters, that is, RG665 and BG3, both of which are so-called glass filters.

We put the glass filter on top of the fish-eye lens and succeeded in removing most of the contributions of 557.7 and 630.0 nm emissions. Figure 2 shows the transmission characteristics of the RG665 (orange) and BG3 (purple) glass filters. We also plot the quantum efficiency (QE) of the EMCCD camera with the gray line. Note that the transmittance values from the specification sheet remain greater than 75% beyond 1,000 nm for both the filters although the transmittance data in Figure 2 obtained at the laboratory experiment only covers wavelengths from 350 to 750 nm for RG665 and from 300 to 850 nm for BG3. Transmission of both the filters can cut the 557.7 and 630.0 nm lines, yet passes prompt emissions. In the first year of measurement, we employed the RG665 filter at all the stations. As shown in Figure 2, the RG665 glass filter covers prompt emissions of nitrogen molecules extending from ∼600 nm to beyond 1,000 nm (so-called N_2 1PG band emissions). However, there still exists a small contribution from the O(^{1}D) emission at 630.0 nm. Since the start of the second winter season from September 2017, we have been using the BG3 filter which completely removes the contribution of 630.0 nm.

In this case, one of the main components is the so-called N_2^+ 1NG emission at 427.8 nm (blue vertical line in Figure 2). But, the BG3 filter is also able to capture several prompt emissions of N_2 1PG existing in near-infrared areas from 700 to 900 nm since the quantum efficiency of the EMCCD camera is still ~50% at 850 nm. Recently, spectral observations of PsA were reported by Tsuda et al. (2020) who demonstrated that the luminosity of the N_2 1PG emissions in the range of 600–900 nm actually pulsates during PsA. This result implies that a number of N_2 1PG band emissions beyond 600 nm have significant contributions for both the cases of RG665 and BG3 filters. In contrast, the N_2 2PG emissions in 300–400 nm are relatively insignificant because the QE is less than 50% in these wavelengths.

We have installed the 100 Hz ASIs in four places in Scandinavia and two places in Alaska. The ASIs in Kevo, Gakona and Poker Flat were deployed by a joint effort with the PWING project (Shiokawa et al., 2017). The locations (i.e., geographic latitude, geographic longitude and magnetic latitude: MLAT) of the six stations are summarized in Table 1. Figure 3 shows the field-of-view (FOV) coverage of these ASIs in the geographic coordinate system with an assumption of the emission altitude at 110 km, where the contours of AACGM magnetic latitude (Baker & Wing, 1989) are overplotted. In both the panels, the statistical location of the auroral oval for Kp = 4 is superimposed (Feldsten & Starkov, 1967). As shown in Figure 3a, the FOVs of the four EMCCD ASIs in Tromsø, Kevo, Tjautjas and Sodankylä, whose FOVs are depicted respectively by the four red circles, construct a network of optical observations covering from 15° to 35° in longitude and 64° to 73° in latitude. In particular, the ASIs cover the equatorward part of the statistical auroral oval where frequent appearance of PsA is expected. In support of the observations with the 100 Hz ASIs, all-sky Watec Monochromatic Imagers (WMIs: Ogawa et al., 2020a) have been complementarily deployed at six locations in northern Scandinavia. The fields-of-view of the WMIs at Tromsø, Skibotn, Kilpisjarvi, Kiruna, Tjautjas and Sodankylä are plotted with the green circles in Figure 3a.

In Alaska, we have been operating two 100 Hz sampling EMCCD ASIs in Gakona and Poker Flat. As shown in Figure 3b, the FOVs of these two ASIs cover a region extending in the latitudinal direction (from 59° to 69° MLAT) including the viewing area of the Poker Flat Incoherent Scatter Radar (PFISR). The coverage of the ASI in Gakona extends down to 59° MLAT, which may enable us to observe optical manifestation of microbursts in the subauroral latitudes.

2.2. 10 Hz All-Sky Imagers

In addition to the 100 Hz sampling high-speed ASIs, we have been operating two monochromatic ASIs at the EISCAT radar facility in Tromsø, which are equipped with narrow band-pass optical filters for observing specific aurora emissions. The purpose of this monochromatic observation is to derive the characteristic energy of precipitating electrons from the intensity of two auroral emission lines. Since we need to observe optical emissions in much narrower wavelength, that is, the incoming flux of photons is much more limited compared to that of the 100 Hz ASIs, the exposure time and corresponding temporal resolution (sampling interval) become longer, which have been 10 Hz for the monochromatic ASIs. This 10 Hz frame rate was determined by considering the longest interval that can detect the internal modulation of PsA, which is normally 3 Hz.

The system is composed of two identical ASIs equipped with different optical filters. The ASI-2 optics of Nikon developed by Taguchi et al. (2004) are combined with the same EMCCD cameras (C9100-23B of Hamamatsu Photonics). The EMCCD cameras capture an image when it is externally triggered. These external triggering pulses are delivered from a USB-SG trigger unit directly connected to the PC. The camera captures 100 msec exposure images 10 times in a second. Since the exposure time of this monochromatic observation is 10 times longer than that of the 100 Hz high-speed ASIs, the USB-SG is triggered by the control PC once a minute and the USB-SG triggers the camera 600 times following a trigger from the PC (i.e., 10 times in a second). The image capturing/saving procedure is the same as that of the 100 Hz ASIs, but the size of one raw file compiling 600 images (256 × 256 pixels) in a minute is only ~75 MB.

There are several auroral emissions that can be used for estimating the energy of precipitating electrons, for example, 427.8 nm, N_2 1PG between 650 and 700 nm, 777.4 and 844.6 nm (e.g., Lanchester et al., 1994; Ono, 1993). The basic idea is that we estimate the characteristic energy of precipitating electrons by using the ratio of emission intensities at two different wavelengths. If we consider a pair of emissions at 427.8 and 844.6 nm, the N_2^+ 1NG emission at 427.8 nm is mainly caused by relatively harder electron precipitation while the oxygen emission at

Journal of Geophysical Research: Space Physics
10.1029/2023JA031527

Table 1
Geographic and Magnetic Coordinates (AACGM) of the Six Stations in Scandinavia and Alaska

Station (ID)	Instruments			
Operation period	High speed ASI	Monochromatic ASI	Photometer	Magnetometer
Tromsø, Norway (TRO)		Glat: 69.58, Glon: 19.23, MLAT: 66.76		
20160925 to 20170126		10 Hz @ 427.8 nm as Cam5		20 Hz sampling
		10 Hz @ 777.4 nm as Cam1		
		10 Hz @ 844.6 nm as Cam3		
20170128 to 20170416	100 Hz @ RG665 as Cam1	10 Hz @ 427.8 nm as Cam5	20 Hz sampling	
		10 Hz @ N2 1PG as Cam4		
		10 Hz @ 844.6 nm as Cam3		
20170902 -	100 Hz @ BG3 as Cam1	10 Hz @ 427.8 nm as Cam5	400 Hz sampling	
		10 Hz @ 844.6 nm as Cam3		
Sodankylä, Finland (SOD)		Glat: 67.37, Glon: 26.63, MLAT: 64.19		
20160926 to 20170423	100 Hz @ RG665 as Cam2			
20170918 -	100 Hz @ BG3 as Cam2			
Tjautjas, Sweden (TJA)		Glat: 67.31, Glon: 20.73, MLAT: 64.39		
20170906 -	100 Hz @ BG3 as Cam4			
Kevo, Finland (KEV)		Glat: 69.76, Glon: 27.01, MLAT: 66.57		
20170129 to 20170415	100 Hz @ RG665 as Cam6			
20170831 -	100 Hz @ BG3 as Cam6			
Gakona, Alaska, USA (GAK)		Glat: 62.39, Glon: 214.78, MLAT: 63.32		
20170304 to 20170503	100 Hz @ RG665 as Cam7			
20170928 -	100 Hz @ BG3 as Cam7			
Pokar Flat, Alaska, USA (PFRR)		Glat: 65.13, Glon: 212.51, MLAT: 65.65		
20180830 -	100 Hz @ BG3 as Cam8			

Note. The settings (selection of optical filter and sampling rate) of the instruments are also given.

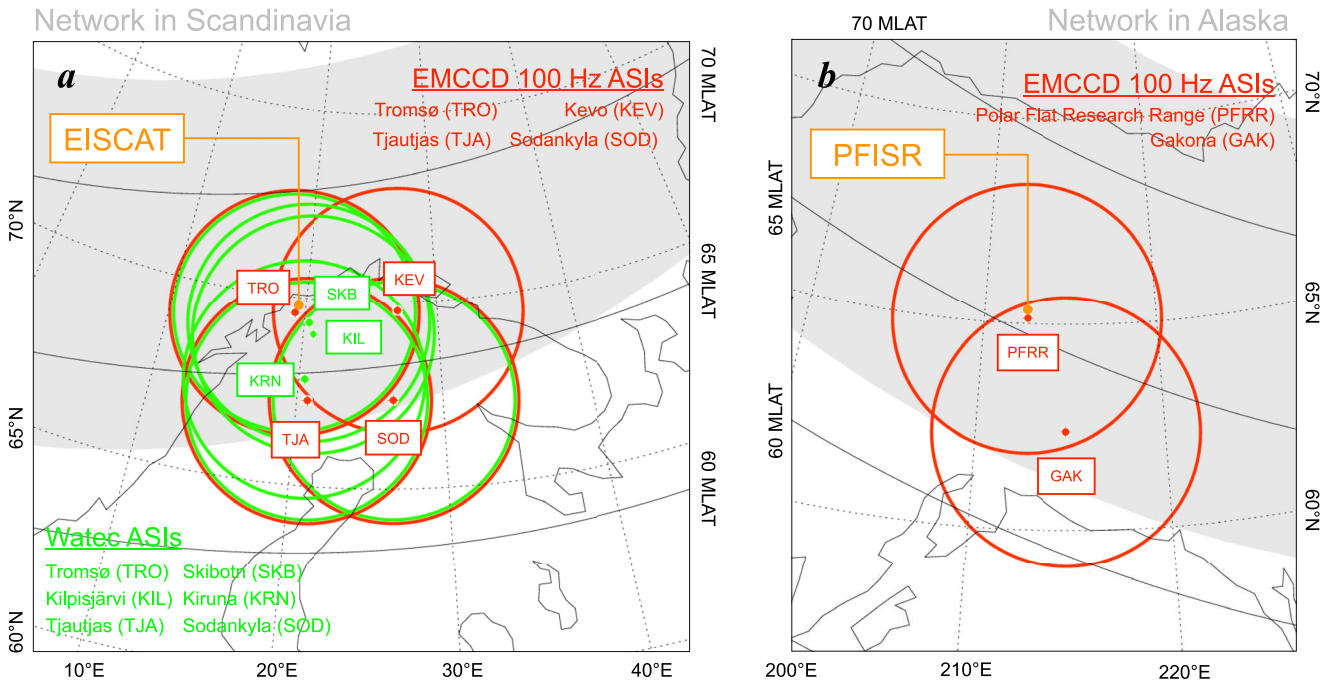

Figure 3. Fields-of-view of the ASIs (a) in the Scandinavian sector and (b) in Alaskan sector. The contours of AACGM magnetic latitude (Baker & Wing, 1989) are overplotted. In both the panels, the auroral oval modeled by Feldsten and Starkov (1967) is depicted for Kp = 4 case.

844.6 nm is more associated with softer electrons; thus, the ratio of 427.8 nm emission to that of 844.6 nm emission can be used as a proxy for the characteristic energy of incoming electrons. This two wavelengths method has been used by many studies such as Ono (1993) and Lanchester et al. (1994).

The emissions we have considered are 427.8 nm, N_2 1PG (650–700 nm), 777.4 and 844.6 nm emissions. All of these emissions are prompt emission; thus, we do not need to consider any time delays of the emission from the collisional excitation by the precipitating electrons. When we started the 10 Hz monochromatic ASI observations, we did not know which pair of the emissions is the best combination to be used for the energy estimation. Then, we operated four identical monochromatic ASIs in the same place (in Tromsø) and tried to determine the best pair of the emissions for estimating the energy of PsA electrons. The results are described in detail in Oyama et al. (2018), but it was found that the emission at 777.4 nm, which was originally considered as an emission representing low-energy component of PsA precipitation, can also be caused by relatively harder precipitations. This means that the use of 777.4 nm is not appropriate for the two wavelengths method. The N_2 1PG band emission extending from 650 to 700 nm is composed of five bands in this range, and the emission model of GLOW (Solomon, 2017) is not able to model these wavelengths. By considering these factors, we eventually decided to use 427.8 nm as a proxy for the harder precipitation and 844.6 nm as that for softer precipitation. Selection of optical filters for the 10 Hz monochromatic ASIs in Tromsø is summarized in Table 1. As mentioned above, we tested 777.4 nm and N_2 1PG emissions during the first season from September 2016 to April 2017. Since the beginning of the second winter season from September 2017, we have only observed 427.8 and 844.6 nm emissions.

The calibration of the 10 Hz ASIs has regularly been carried out by using data from 5 channel photometer in Tromsø (Nozawa et al., 2018). Since the deployment, the photometer was calibrated using an integrating sphere at National Institute of Polar Research, Japan once a year during summer months when the optical observations are resumed; thus, the cross-calibration between the 10 Hz ASIs and the photometer enables us to derive the absolute optical intensity for the 10 Hz ASI images in units of Rayleigh.

2.3. 20 Hz Fluxgate Magnetometer Observations

The 20 Hz magnetometer consists of a sensor, a GPS (Global Positioning System) receiver, a magnetometer electronics unit, and a PC. The dimensions of the magnetometer sensor part (MAG-03TB) developed by Bartington

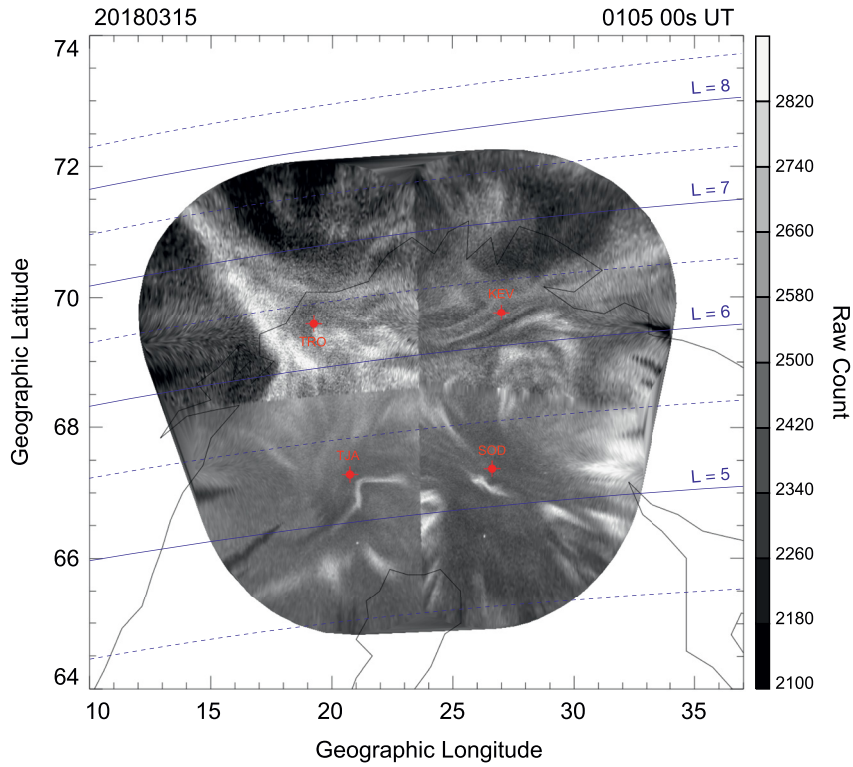

Figure 4. Example of the multi-point observations of PsA by the four 100 Hz sampling EMCCD ASIs in Scandinavia which was obtained at 01:05 UT on 15 March 2018.

Instruments Ltd. are diameter of 280 mm and height of 110 mm. This magnetometer system can observe three orthogonal components of the geomagnetic field with a dynamic range of ±70,000 nT and the resolution of less than 1 nT. The typical noise intensity at 1 Hz is 6 pT/Hz$^{1/2}$, and the mean square level of the noise is 0.2 nT p-p in the frequency band of 0.01–1 Hz. The GPS system with a time accuracy of less than ±1μ sec provides 1PPS to the AD converter of the magnetometer and synchronizes the time stamp in the magnetometer data, which is sufficient for the current sampling rate at 20 Hz. The DCA-500BA magnetometer electronics units made by TIERRA TECNICA Ltd. are equipped with Linux Arm11. The magnetometer data are stored in the internal flash memory with a sampling rate of 20 Hz and transferred to a data server in Japan once a day. We installed the magnetic field sensor in a small house and adjusted the X, Y, and Z components to northward (geomagnetic), eastward (geomagnetic), and downward directions, respectively. The sensor is connected to the magnetometer electronics units with a 70 m cable covered with plastic tubes. The magnetometer electronics units and the PC were installed in an observation building, in which the EMCCD ASIs are operative. The GPS receiver, which provides precise time information for the magnetometer, was mounted to the exterior wall of the main house.

3. Observations

3.1. Example of 100 Hz Observations

Figure 4 shows an example of the multi-point observations of PsA from the four EMCCD ASI stations (TRO, TJA, KEV and SOD) in Scandinavia which was obtained at 01:05 UT on 15 March 2018. To make this plot, we have integrated the original 100 Hz images with a sampling rate of 25 Hz to reduce the random noise typical in the low-light condition measurement with EMCCD cameras. It might be difficult to see only from this static image, but there are a number of patches of PsA within the FOVs of all the four ASIs. The latitudinal coverage of the combined FOV extends from 65° to 72° geographic latitude, which corresponds to an *L* value range from ~4.5 to almost 7.5. During the interval surrounding this image, we detected both the main pulsation and internal modulations at some of the stations. Two movies attached to the electronic version of this article more clearly demonstrate the behaviors of the main pulsation and internal modulation, respectively. The main pulsation is

visualized in the Movie S1 which is a 1-hr animation made from 1 s averaged optical data from the four stations. Movie S2, which is a 1-min animation with the 25 Hz frame rate, shows how the internal modulations are seen in the sub-second time-scale. Note that Movie S2 is a real-time movie; thus, all the fluctuating signatures seen in the movie, which are more evident within the FOVs of the two ASIs at lower latitude (Sodankylä and Tjautjas), are the internal modulations.

Figure 5 displays the temporal variations of PsA obtained by the 100 Hz ASI in Tjautjas, Sweden during the interval of simultaneous observations of PsA in Scandinavia on 15 March 2018 (Figure 4). Figure 5a is the time-series of optical data in a format of south to north keogram. The keogram is filled with a number of vertical stripes, most of which are signatures of the main pulsation. Figure 5b is a zoom-in view of the 1-min optical data within the green box in the southern half of Figure 5a. In a region near the horizontal red line, nine enhancements of optical intensity are seen, which are manifestations of the main pulsation. In this case, the periodicity of the main pulsation is 6–10 s. The zoom-in keogram also indicates an existence of short time-scale streaks embedded within the ON phase of the main pulsation. These thin stripes are the signatures of sub-second internal modulation of PsA. Figure 5c shows two time-series of the raw count sampled along the red and blue lines in Figure 5b. It is clearly seen that there are several tiny peaks on the plateau of the main pulsation, which are the manifestation of the internal modulation. Note that there exist fluctuations even during the OFF phase of the main pulsation which are considered to be the noise component typical for short exposure time EMCCD observations. The signatures of the internal modulation are identified as relatively larger peaks on the plateaus, which are more clearly seen in the blue line in Figure 5c. Figure 5d shows the high frequency component of the optical intensity produced by subtracting 1 s running average of the original time-series (Figure 5c). During the ON phases of the main pulsation, the amplitude of high-frequency fluctuation is larger which proves that the spiky peaks on the plateau of the main pulsation correspond to the signatures of internal modulation rather than instrumental noises.

One of the primary purposes of the current observations is to conduct ground-satellite conjugate observations of PsA, especially simultaneous measurements with the Arase satellite, which was launched in December 2016. The wave instruments onboard Arase, the Plasma Wave Experiment (PWE) (Y. asahara et al., 2018), are capable of so-called "burst mode operation" with 64 kHz sampling rate in limited time intervals (Matsuda et al., 2018). To find good intervals for simultaneous observations using the burst mode, we made a website showing conjunctions between the FOVs of various ground-based instruments at high-latitudes and the magnetic footprints of Arase. The website (https://ergsc.isee.nagoya-u.ac.jp/psa-gnd/bin/cif.cgi), which is called Conjunction Interval Finder (CIF), has been operative at the ERG Science Center at Nagoya University (Miyoshi, Hori, et al., 2018) since the start of the routine observation of Arase.

Figure 6 shows how CIF provides information about the conjunctions. In the top row, conjunctions between Arase and stations at the auroral latitudes (Scandinavia, Iceland, Antarctic Syowa Station, and Alaska) are displayed. In the middle two rows, conjunctions at the subauroral latitudes (most of them are the PWING sites) are shown. In the bottom row, conjunctions with the incoherent scatter radars (EISCAT, Kharkiv, PFISR, Millstone Hill and PANSY) are shown. In all the panels, the magnetic footprints of Arase derived by tracing the IGRF magnetic field lines are plotted where the color of the points represents MLT of the footprint. That is, bluish footprints mean morning side observations (00–06 MLT), which is favorable for the studies of PsA. The satellite positioning data (predicted orbit data) and corresponding plots are refreshed every day. This website also offers a capability of showing plots from previous/future periods. Users can browse the interval of their interest by specifying the date on top of the page. This further enables the users to check the conjunctions for the interval of their interest but also for considering the timing of burst mode operation of the satellite.

3.2. Example of Multi-Wavelength Observations

Figure 7 summarizes an example of multi-spectral observations of PsA during a 5 min interval from 03:22 to 03:27 UT on 6 March 2017. In this interval, two auroral emissions at 844.6 nm (Figure 7a) and 427.8 nm (Figure 7b) were observed respectively by the two identical ASI systems with a temporal resolution of 10 Hz. The original raw count data have been converted to Rayleigh through the procedure described in Ogawa et al. (2020a, 2020b). In the keograms of both emissions, weak vertical stripes are seen which are manifestations of the main pulsation of PsA. The two lines in Figure 7c respectively show the time-series of optical intensity at the horizontal red/blue lines in the keograms. To derive these time-series, the original 10 Hz data are spatially averaged with 3×3 pixels spatial window and moving average with an window of 1 s. This spatial/temporal averaging process makes

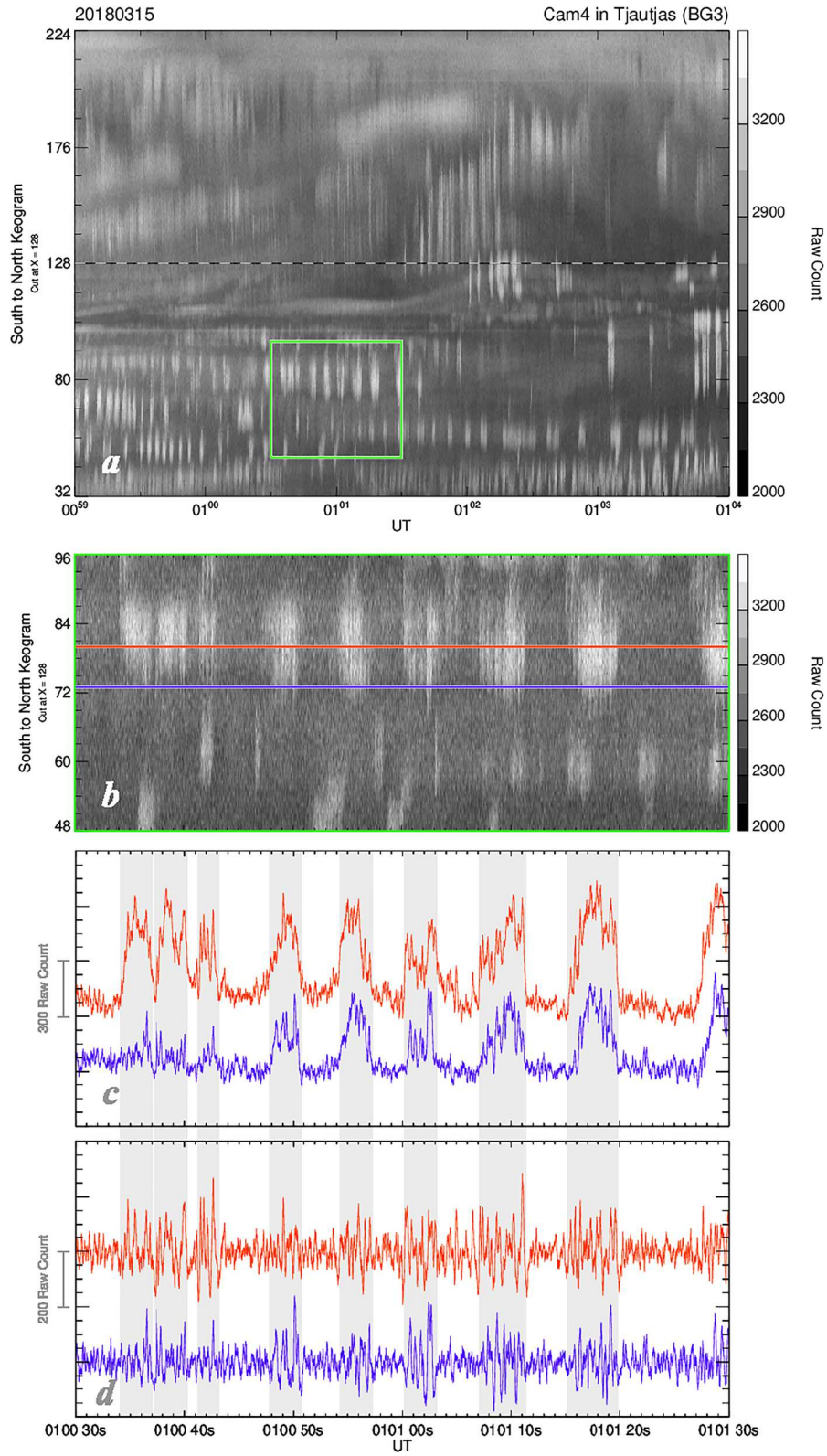

Figure 5. Temporal variations of PsA obtained by the 100 Hz ASI in Tjautjas, Sweden during the interval of simultaneous observations of PsA in Scandinavia on 15 March 2018, (a) the time-series of optical data from 00:59 to 01:04 UT in a format of south to north keogram, (b) zoom-in view of the 1-min optical data within the green box in the southern half of Figure 6a, (c) two time-series of the raw count sampled along the red and blue lines in Figure 6b, (d) high-frequency component of the time-series in Figure 6c derived by subtracting 1 s moving average of the original time-series.

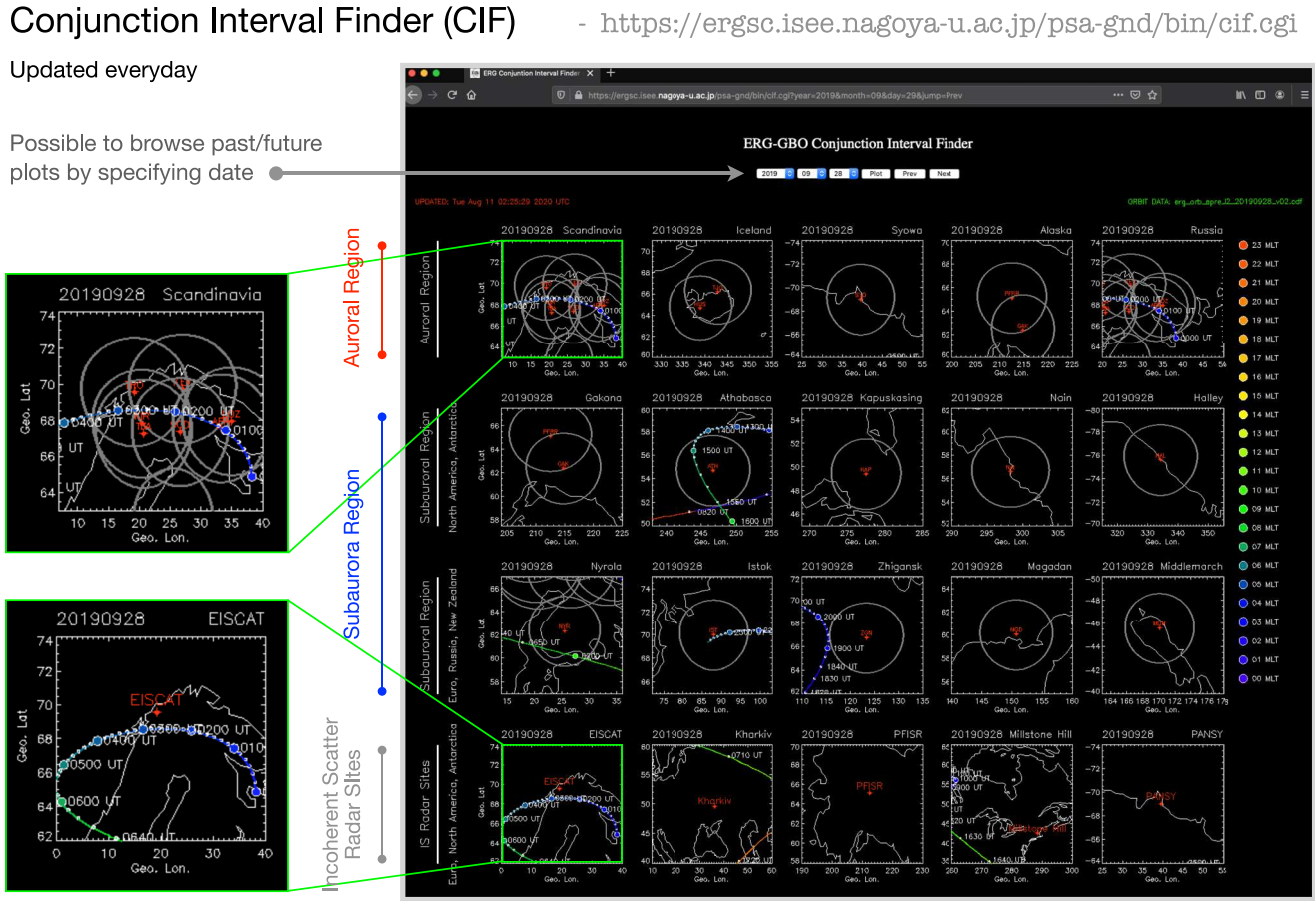

Figure 6. Conjunction Interval Finder (CIF) operated by the ERG Science Center at Nagoya University (https://ergsc.isee.nagoya-u.ac.jp/psa-gnd/bin/cif.cgi).

the main pulsation of PsA visible through reduction of unwanted random noise. Important point is that the 10 Hz monochromatic ASI observations were able to detect the main pulsation of PsA in both the 427.8 and 844.6 nm emissions. This combination can be used to estimate the energy of precipitation electrons during the ON and OFF phases of PsA by using a method introduced by Ono (1993) or by comparing the data with those estimated by the optical emission model such as GLOW (Solomon, 2017).

The energy of precipitating electrons causing PsA is one of the fundamental parameters characterizing the process of wave particle interaction (WPI). For example, the energy of PsA electrons can be used to infer the resonance energy of the first-order cyclotron resonance (Kennel & Petschek, 1966). The information about the energy can also be used for determining how far the region of WPI is located away from the magnetic equator (Miyoshi et al., 2010, 2015b, 2020). We might be able to observe a systematic change in the characteristic energy of electrons during a single main pulse of PsA, which can be interpreted by the time-of-flight effect of precipitating electrons (e.g., Miyoshi et al., 2010, 2015b, 2020). In those senses, it is of particular importance in the studies of PsA to estimate the characteristic energy of electrons using the two wavelengths method. Interesting thing to note is that the two time-series of 427.8 and 844.6 nm in Figure 7c are slightly different, which might be a result of the change of energy during a single ON phase of the main pulsation. By looking at such a difference in the two emissions it would be possible to discuss the temporal evolution of the WPI process at least in the time-scale of the main pulsation.

3.3. Optical, Radar and Geomagnetic Field Observations of PsA in Tromsø

Here, we introduce an integrated observation of PsA by combining data from the ground-based ASIs, magnetometer and EISCAT radar in Tromsø, Norway. On the night of 17 February 2018, we conducted a campaign observation of PsA by using the EISCAT UHF radar in combination with the EMCCD ASIs and magnetometer in Tromsø. Figure 8 shows a summary of the measurements during a 10 min interval from 02:10 to 02:20 UT. The top panel shows the 100 Hz ASI data in the format of south to north keogram where the horizontal dashed

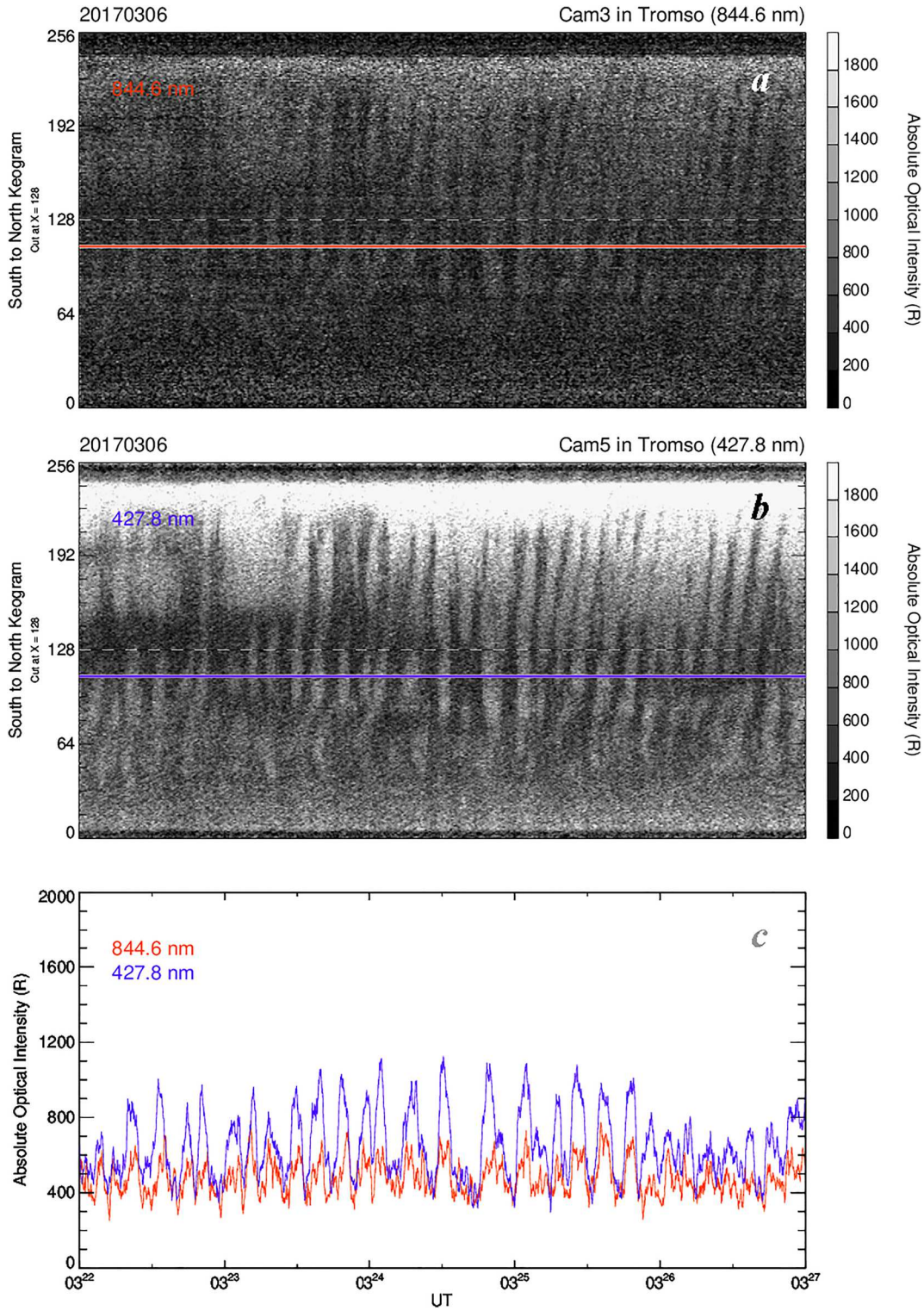

Figure 7. 10 Hz Monochromatic ASI observations during a 5 min interval from 03:22 to 03:27 UT on 6 March 2017. (a, b) South to north keogram of 844.6 and 427.8 nm emissions where the horizontal dashed lines in the keograms mark the center of the image which corresponds to the zenith, (c) time-series of the optical intensities at the horizontal lines in the keograms.

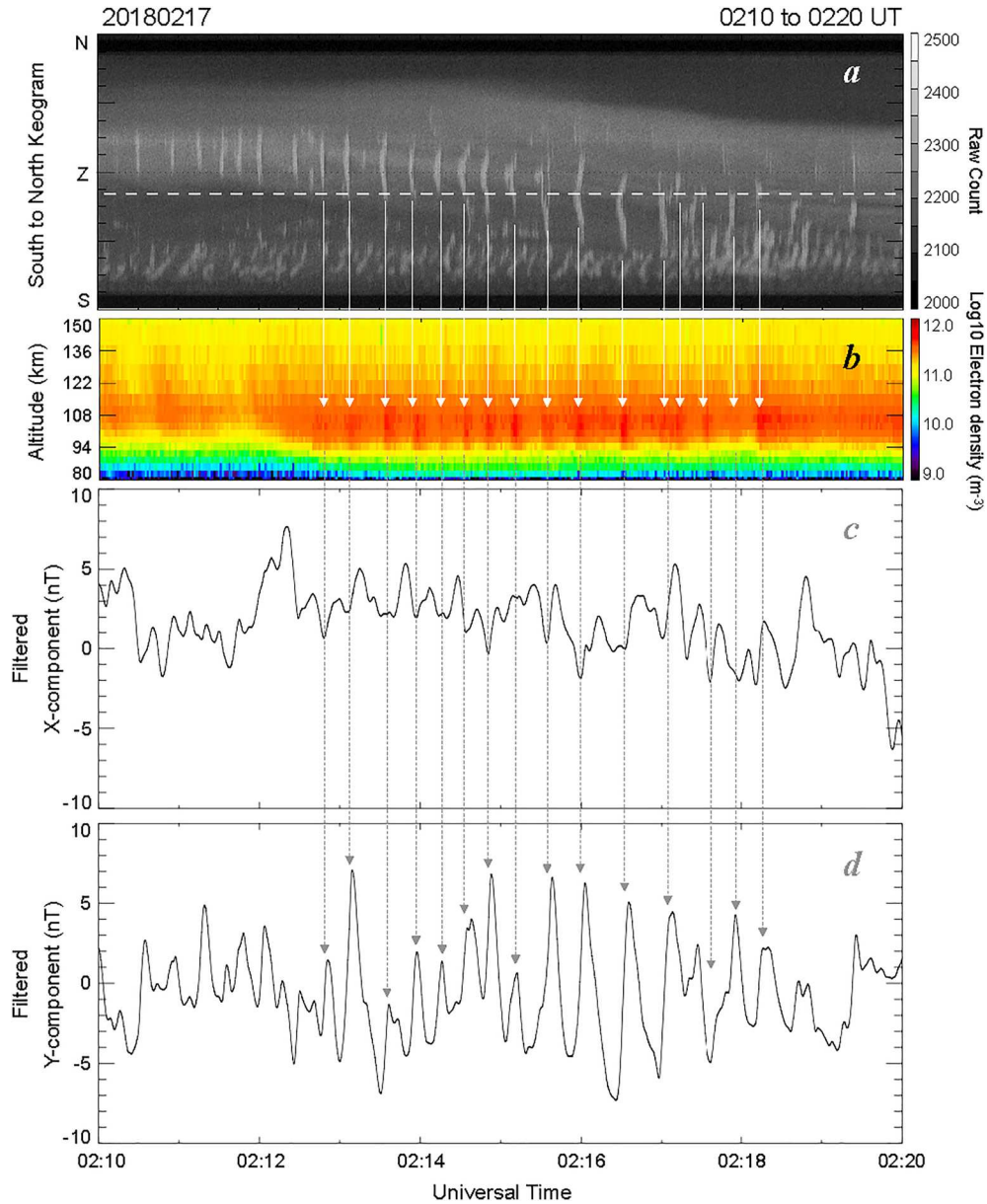

Figure 8. Simultaneous optical, electron density and magnetic field observations in Tromsø, Norway on 17 February 2018. (a) South to north keogram made from the 100 Hz ASI images where the sensing area of the EISCAT UHF radar (field-aligned direction) is drawn with the horizontal dashed line. (b) Altitude-time plot of electron density from EISCAT, (c, d) residual of the X and Y component of magnetic field in Tromsø.

line shows the position of the field-aligned beam of the CP1 observation mode of EISCAT UHF radar. The keogram well demonstrates successive appearances of stripes in the vicinity of the sensing area of EISCAT which are manifestations of the main pulsation of PsA. Figure 8b shows the altitude-time plot of the electron density obtained from the EISCAT UHF radar. The electron density in the E region altitude (say from 90 to 120 km) exhibits a characteristic modulation, which corresponds to the optical pulsation seen in Figure 8a. The bottom two panels of Figure 8 respectively display the residual of the X (northward) and Y (eastward) components of ground-based magnetic field observations. The comparison with the optical and electron density data indicates that the X (Y) component decreases (increases) when PsA becomes ON.

As shown in Figure 8, coherent magnetic field pulsation was seen during the interval of PsA. The EISCAT radar, at the same time, identified a variation in the electron density showing similar periodic signatures. These

simultaneous observations confirm the origin of magnetic field pulsation during PsA. First the temporal variation in the flux of electron precipitation during PsA produces a pulsation in the electron density. The pulsation in the electron density then modulates the ionospheric current flowing in the horizontal direction through changes in the conductance. Eventually, modified ionospheric current generates pulsation in the magnetic field on the ground. This idea was initially implied by Arnoldy et al. (1982), Oguti and Hayashi (1984), and Oguti et al. (1986), but it has been difficult to prove it by comparing simultaneous observations of the optical intensity, electron density, and ground magnetic field with sufficiently high temporal resolution. Recent high-time resolution EISCAT observations enabled us to derive the conductivity variation with a temporal resolution which can resolve the main pulsation (e.g., Hosokawa et al., 2010). The combination of such high-time resolution optical, magnetic field and conductivity observations allows us to reveal the change of ionospheric current system during the episodes of PsA (i.e., ON and OFF phases of the main pulsation) following a mechanism for example, discussed by Hosokawa et al. (2010).

4. Summary

We have developed and deployed a set of scientific equipment for studying pulsating aurora. The system is composed of the following instruments:

1. High-speed EMCCD ASIs at 100 Hz sampling at six stations in Scandinavia and Alaska
2. Two monochromatic EMCCD ASIs at 10 Hz sampling rate in Tromsø, which mainly observe the 427.8 and 844.6 nm emissions
3. A 20 Hz sampling ground-based fluxgate magnetometer in Tromsø

The six high-speed EMCCD ASIs are mainly used for visualizing the fine-scale temporal characteristics of PsA in a wide area, especially during conjunction observations of the Arase satellite. The monochromatic ASI systems are used for estimating the energy of precipitating PsA electrons with a support of 5-channel photometer as a calibration standard. The high-time resolution fluxgate magnetometer will be intensively used for observing rapid changes in the ionospheric current system during the ON/OFF phases of PsA in combination with simultaneous observations of the ionospheric electron density (i.e., conductance) by the EISCAT radar in Tromsø.

The raw data files from the 100 Hz EMCCD ASIs are downloadable from a site at https://ergsc.isee.nagoya-u.ac.jp/psa-gnd/pub/raw within the ERG Science Center. The software written in IDL (Interactive Data Language) for reading and plotting the raw data files is also available at https://ergsc.isee.nagoya-u.ac.jp/psa-gnd/pub/raw/soft/. The software can run with/without SPEDAS (Space Physics Environment Data Analysis System: Angelopoulos et al., 2019) environment. CDF format data files with a temporal resolution of 10 Hz are currently being produced from the original 100 Hz raw data. The 10 Hz CDF format data (including 20 Hz photometer data) will become downloadable at https://ergsc.isee.nagoya-u.ac.jp/psa-gnd/pub/cdf/. All the data for quick look are available at https://ergsc.isee.nagoya-u.ac.jp/psa-gnd/bin/psa.cgi, where keograms and digest movies can be browsed. The detailed information about the quality of the ASIs (both 100 and 10 Hz) and magnetometer data is described and regularly updated at https://ergsc.isee.nagoya-u.ac.jp/psa-gnd/pub/raw/operation_note.txt.

Continuous efforts will be taken to keep the entire PsA observation system operative during the next solar cycles. The high-speed 100 Hz ASI data have been used for conjunction measurements with the Arase satellite (e.g., Fukizawa et al., 2018; Hosokawa et al., 2020; Ozaki et al., 2019). Good conjunctions are still expected in the coming winter seasons in the northern hemisphere. Now the EISCAT_3D system (e.g., McCrea et al., 2015) is being constructed in northern Scandinavia, which will be the largest incoherent scatter radar system in the world when fully operated. At least three high-speed ASIs have a common FOV with the core-site antenna at Skibotn, Norway. EISCAT_3D will provide high-time resolution data of electron density and ion velocity in 3D, which will be compared with the high-speed optical data in the surrounding area. In the framework of the collaboration with EISCAT_3D, targets of measurements are not only PsA but also other kinds of aurora such as discrete aurora and flickering aurora.

Data Availability Statement

The data from the Arase (ERG) satellite and ground-based instruments were obtained from the ERG Science Center operated by the Institute of Space and Astronautical Science of the Japan Aerospace eXploration Agency and the Institute for Space-Earth Environmental Research of Nagoya University (https://ergsc.isee.nagoya-u.

ac.jp/index.shtml.en, Miyoshi, Hori, et al., 2018). The EMCCD all-sky camera data are accessible at the following DOIs, 100 Hz ASI at Tromsø station: https://doi.org/10.34515/DATA.GND-0059-0006-0201_v01, 100 Hz ASI Sodankylä: https://doi.org/10.34515/DATA.GND-0049-0006-0202_v01, 10 Hz monochromatic (844.6 nm) ASI Tromsø: https://doi.org/10.34515/DATA.GND-0059-0006-0203_v01, 100 Hz ASI at Tjautjas: https://doi.org/10.34515/DATA.GND-0062-0006-0204_v01, 10 Hz monochromatic (427.8 nm) ASI at Tromsø: https://doi.org/10.34515/DATA.GND-0059-0006-0205_v01, 100 Hz ASI at Kevo: https://doi.org/10.34515/DATA.GND-0022-0006-0206_v01, 100 Hz at Gakona station: https://doi.org/10.34515/DATA.GND-0013-0006-0207_v01, and 100 Hz ASI at Pokar Flat: https://doi.org/10.34515/DATA.GND-0040-0006-0208_v01.

Acknowledgments

K.H, S.O, Y.O, Y.M and Y.T are supported by JSPS Kakenhi (22H00173). Y.T, K.H, and Y.O are supported by JSPS Kakenhi (21H01152). K.H, S.O and Y.T are supported by JSPS Kakenhi (21KK0059). M.O, Y.O, Y.T and K.H are supported by JSPS Kakenhi (20H02162). K.H., S.O., Y.O. Y.M. and R.F. are supported by JSPS Kakenhi (15H05747). Y.M. and R.K. are supported by JSPS Kakenhi (15H05815). S.O., Y.M., S.K., R.K. and K.S. are supported by JSPS Kakenhi (16H06286). K.H., Y.M. and S.K. are supported by the International Space Science Institutes Beijing (ISSI-BJ) International Team program. Y.K. is supported by JSPS Kakenhi (16H04056 and 16H01172). The operation of the instruments in Tromsø has been supported by Tromsø Geophysical Observatory (TGO), the Arctic University of Norway (UiT). The operation of the ASIs in Sodankylä has been supported by the Sodankylä Geophysical Observatory (SGO). The operation of the ASIs in Tjautjas has been supported by the Swedish Institute of Space Physics (IRF). The operation of the EMCCD ASI in Kevo has been supported by the Finnish Meteorological Institute (FMI) and Turku University. The operation of the EMCCD ASIs in Gakona and Poker Flat Research Range, Alaska, has been supported by the University of Alaska Fairbanks (UAF).

References

Angelopoulos, V., Cruce, P., Drozdov, A., Grimes, E. W., Hatzigeorgiu, N., King, D. A., et al. (2019). The space physics environment data analysis system (SPEDAS). *Space Science Reviews*, *215*(1), 9. https://doi.org/10.1007/s11214-018-0576-4

Arnoldy, R. L., Dragoon, K., Cahill, L. J., Mende, S. B., Jr., & Rosenberg, T. J. (1982). Detailed correlations of magnetic field and riometer observations at L = 4.2 with pulsating aurora. *Journal of Geophysical Research*, *87*(A12), 10449–10456. https://doi.org/10.1029/JA087iA12p10449

Baker, K. B., & Wing, S. (1989). A new magnetic coordinate system for conjugate studies of high latitudes. *Journal of Geophysical Research*, *94*(A7), 9139. https://doi.org/10.1029/ja094ia07p09139

Demekhov, A. G., & Trakhtengerts, V. Y. (1994). A mechanism of formation of pulsating aurorae. *Journal of Geophysical Research*, *99*(A4), 5831–5841. https://doi.org/10.1029/93JA01804

Feldsten, Y. I., & Starkov, G. V. (1967). Dynamics of auroral belt and polar geomagnetic disturbance. *Planetary and Space Science*, *15*, 209–229. https://doi.org/10.1016/0032-0633(67)90190-0

Foster, J. C., Erickson, P. J., Omura, Y., Baker, D. N., Kletzing, C. A., & Claudepierre, S. G. (2017). Van Allen Probes observations of prompt MeV radiation belt electron acceleration in nonlinear interactions with VLF chorus. *Journal of Geophysical Research: Space Physics*, *122*(1), 324–339. https://doi.org/10.1002/2016ja023429

Foster, J. C., & Rosenberg, T. J. (1976). Electron precipitation and VLF emissions associated with cyclotron resonance interactions near the plasmapause. *Journal of Geophysical Research*, *81*(13), 2183–2192. https://doi.org/10.1029/ja081i013p02183

Fukizawa, M., Sakanoi, T., Miyoshi, Y., Hosokawa, K., Shiokawa, K., Katoh, Y., et al. (2018). Electrostatic electron cyclotron harmonic waves as a candidate to cause pulsating auroras. *Geophysical Research Letters*, *45*(23), 12661–12668. https://doi.org/10.1029/2018GL080145

Hosokawa, K., Miyoshi, Y., & Li, W. (2015). Introduction to special section on pulsating aurora and related magnetospheric phenomena. *Journal of Geophysical Research: Space Physics*, *120*(7), 5341–5343. https://doi.org/10.1002/2015JA021453

Hosokawa, K., Miyoshi, Y., Ozaki, M., Oyama, S.-I., Ogawa, Y., Kurita, S., et al. (2020). Multiple time-scale beats in aurora: Precise orchestration via magnetospheric chorus waves. *Nature Scientific Report*, *10*(1), 3380. https://doi.org/10.1038/s41598-020-59642-8

Hosokawa, K., Ogawa, Y., Kadokura, A., Miyaoka, H., & Sato, N. (2010). Modulation of ionospheric conductance and electric field associated with pulsating aurora. *Journal of Geophysical Research*, *115*(A3), A03201. https://doi.org/10.1029/2009JA014683

Jones, A. V. (1974). *Aurora*. Reidel Publishing Company. https://doi.org/10.1007/978-94-010-2099-2

Kasahara, S., Miyoshi, Y., Yokota, S., Mitani, T., Kasahara, Y., Matsuda, S., et al. (2018a). Pulsating aurora from electron scattering by chorus waves. *Nature*, *554*(7692), 337–340. https://doi.org/10.1038/nature25505

Kasahara, Y., Kasaba, Y., Kojima, H., Yagitani, S., Ishisaka, K., Kumamoto, A., et al. (2018b). The plasma wave experiment (PWE) on board the Arase (ERG) satellite. *Earth Planets and Space*, *70*(1), 86. https://doi.org/10.1186/s40623-018-0842-4

Kataoka, R., Miyoshi, Y., Hampton, D., Ishii, T., & Kozako, H. (2012). Pulsating aurora beyond the ultra-low frequency range. *Journal of Geophysical Research*, *117*(A8), A08336. https://doi.org/10.1029/2012JA017987

Kennel, C. F., & Petschek, H. E. (1966). Limit on stably trapped particle fluxes. *Journal of Geophysical Research*, *71*, 1–28. https://doi.org/10.1029/JZ071i001p00001

Lanchester, B. S., Palmer, J. R., Rees, M. H., Lummerzheim, D., Kaila, K., & Turunen, T. (1994). Energy flux and characteristic energy of an elemental auroral structure. *Geophysical Research Letters*, *21*(25), 2789–2792. https://doi.org/10.1029/94gl01764

Lessard, M. (2012). A review of pulsating aurora. In A. Keiling, E. Donovan, F. Bagenal, & T. Karlsson (Eds.), *Auroral phenomenology and magnetospheric processes: Earth and other planets*. AGU monograph series (Vol. 197). https://doi.org/10.1029/2011GM001187

Matsuda, S., Kasahara, Y., Kojima, H., Kasaba, Y., Yagitani, S., Ozaki, M., et al. (2018). Onboard software of plasma wave experiment aboard arase: Instrument management and signal processing of waveform capture/onboard frequency analyzer. *Earth Planets and Space*, *70*(1), 75. https://doi.org/10.1186/s40623-018-0838-0

McCrea, I. W., Aikio, A., Alfonsi, L., Belova, E., Buchert, S., Clilverd, M., et al. (2015). The science case for the EISCAT_3D radar. *Progress in Earth and Planetary Science*, *2*(1), 21. https://doi.org/10.1186/s40645-015-0051-8

Mende, S. B., Harris, S. E., Frey, H. U., Angelopoulos, V., Russell, C. T., Donovan, E., et al. (2008). The THEMIS array of ground-based observatories for the study of auroral substorms. *Space Science Reviews*, *141*(1–4), 357–387. https://doi.org/10.1007/s11214-008-9380-x

Miyoshi, Y., Hori, T., Shoji, M., Teramoto, M., Chang, T.-F., Segawa, T., et al. (2018). The ERG science center. *Earth Planets and Space*, *70*(1), 96. https://doi.org/10.1186/s40623-018-0867-8

Miyoshi, Y., Hosokawa, K., Kurita, S., Oyama, S.-I., Ogawa, Y., Saito, S., et al. (2021). Penetration of MeV electrons into the mesosphere accompanying pulsating aurorae. *Scientific Reports*, *11*(1), 13724. https://doi.org/10.1038/s41598-021-92611-3

Miyoshi, Y., Katoh, Y., Nishiyama, T., Sakanoi, T., Asamura, K., & Hirahara, M. (2010). Time of flight analysis of pulsating aurora electrons, considering wave-particle interactions with propagating whistler mode waves. *Journal of Geophysical Research*, *115*(A10), A10312. https://doi.org/10.1029/2009JA015127

Miyoshi, Y., Oyama, S., Saito, S., Kurita, S., Fujiwara, H., Kataoka, R., et al. (2015b). Energetic electron precipitation associated with pulsating aurora: EISCAT and Van Allen Probe observations. *Journal of Geophysical Research: Space Physics*, *120*(4), 2754–2766. https://doi.org/10.1002/2014JA020690

Miyoshi, Y., Saito, S., Kurita, S., Asamura, K., Hosokawa, K., Sakanoi, T., et al. (2020). Relativistic electron microbursts as high energy tail of pulsating aurora electrons. *Geophysical Research Letters*, *47*(21), e2020GL090360. https://doi.org/10.1029/2020GL090360

Miyoshi, Y., Saito, S., Seki, K., Nishiyama, T., Kataoka, R., Asamura, K., et al. (2015a). Relation between energy spectra of pulsating aurora electrons and frequency spectra of whistler-mode chorus waves. *Journal of Geophysical Research*, *120*(9), 7728–7736. https://doi.org/10.1002/2015JA021562

Miyoshi, Y., Shinohara, I., Takashima, T., Asamura, K., Higashio, N., Mitani, T., et al. (2018). Geospace exploration project ERG. *Earth Planets and Space*, *70*(1), 101. https://doi.org/10.1186/s40623-018-0862-0

Nishimura, Y., Bortnik, J., Li, W., Thorne, R. M., Lyons, L. R., Angelopoulos, V., et al. (2010). Identifying the driver of pulsating aurora. *Science*, *330*(6000), 81–84. https://doi.org/10.1126/science.1193186

Nishimura, Y., Lessard, M. R., Katoh, Y., Miyoshi, Y., Grono, E., Partamies, N., et al. (2020). Diffuse and pulsating aurora. *Space Science Reviews*, *216*(1), 4. https://doi.org/10.1007/s11214-019-0629-3

Nishiyama, T., Sakanoi, T., Miyoshi, Y., Katoh, Y., Asamura, K., Okano, S., & Hirahara, M. (2011). The source region and its characteristic of pulsating aurora based on the Reimei observations. *Journal of Geophysical Research*, *116*(A3), A03226. https://doi.org/10.1029/2010JA015507

Nozawa, S., Kawabata, T., Hosokawa, K., Ogawa, Y., Tsuda, T., Mizuno, A., et al. (2018). A new five-wavelength photometer operated in Tromsø (69.6°N, 19.2°E). *Earth Planets and Space*, *70*(1), 193. https://doi.org/10.1186/s40623-018-0962-x

Ogawa, Y., Kadokura, A., & Ejiri, M. K. (2020b). Optical calibration system of NIPR for aurora and airglow observations. *Polar Science*, *26*, 100570. https://doi.org/10.1016/j.polar.2020.100570

Ogawa, Y., Tanaka, Y., Kadokura, A., Hosokawa, K., Ebihara, Y., Motoba, T., et al. (2020a). Development of low-cost multi-wavelength imager system for studies of aurora and airglow. *Polar Science*, *23*, 100501. https://doi.org/10.1016/j.polar.2019.100501

Oguti, T., & Hayashi, K. (1984). Multiple correlation between auroral and magnetic pulsations. II - Determination of electric currents and electric fields around a pulsating auroral patch. *Journal of Geophysical Research*, *89*(A9), 7467–7481. https://doi.org/10.1029/JA089iA09p07467

Oguti, T., Hayashi, K., Yamamoto, T., Ishida, J., Higuchi, T., & Nishitani, N. (1986). Absence of hydromagnetic waves in the magnetospheric equatorial region conjugate with pulsating auroras. *Journal of Geophysical Research*, *91*(A12), 13711–13715. https://doi.org/10.1029/JA091iA12p13711

Omura, Y., Hsieh, Y., Foster, J. C., Erickson, P. J., Kletzing, C. A., & Baker, D. N. (2019). Cyclotron acceleration of relativistic electrons through Landau resonance with obliquely propagating whistler-mode chorus emissions. *Journal of Geophysical Research: Space Physics*, *124*, 2795–2810. https://doi.org/10.1029/2018ja026374

Ono, T. (1993). Derivation of energy parameters of precipitating auroral electrons by using the intensity ratios of auroral emissions. *Journal of geomagnetism and geoelectricity*, *45*(6), 455–472. https://doi.org/10.5636/jgg.45.455

Oyama, S., Kero, A., Rodger, C. J., Clilverd, M. A., Miyoshi, Y., Partamies, N., et al. (2017). Energetic electron precipitation and auroral morphology at the substorm recovery phase. *Journal of Geophysical Research: Space Physics*, *122*(6), 6508–6527. https://doi.org/10.1002/2016JA023484

Oyama, S., Tsuda, T. T., Hosokawa, K., Ogawa, Y., Miyoshi, Y., Kurita, S., et al. (2018). Auroral molecular-emission effects on the atomic oxygen line at 777.4 nm. *Earth Planets and Space*, *70*(1), 166. https://doi.org/10.1186/s40623-018-0936-z

Ozaki, M., Miyoshi, Y., Shiokawa, K., Hosokawa, K., Oyama, S., Kataoka, R., et al. (2019). Visualization of rapid electron precipitation via chorus element wave–particle interactions. *Nature Communications*, *10*(1), 257. https://doi.org/10.1038/s41467-018-07996-z

Rosenberg, T. J., Helliwell, R. A., & Katsufrakis, J. P. (1971). Electron precipitation associated with discrete very-low-frequency emissions. *Journal of Geophysical Research*, *76*(34), 8445–8452. https://doi.org/10.1029/ja076i034p08445

Røyrvik, O., & Davis, T. N. (1977). Pulsating aurora: Local and global morphology. *Journal of Geophysical Research*, *82*(29), 4720–4740. https://doi.org/10.1029/ja082i029p04720

Samara, M., & Michell, R. G. (2010). Ground-based observations of diffuse auroral frequencies in the context of whistler mode chorus. *Journal of Geophysical Research*, *115*(A9), A00F18. https://doi.org/10.1029/2009JA014852

Sandahl, I., Eliasson, L., & Lundin, R. (1980). Rocket observations of precipitating electrons over a pulsating aurora. *Geophysical Research Letters*, *7*(5), 309–312. https://doi.org/10.1029/gl007i005p00309

Shiokawa, K., Katoh, Y., Hamaguchi, Y., Yamamoto, Y., Adachi, T., Ozaki, M., et al. (2017). Ground-based instruments of the PWING project to investigate dynamics of the inner magnetosphere at subauroral latitudes as a part of the ERG-ground coordinated observation network. *Earth Planets and Space*, *69*(1), 160. https://doi.org/10.1186/s40623-017-0745-9

Solomon, S. C. (2017). Global modeling of thermospheric airglow in the far ultraviolet. *Journal of Geophysical Research: Space Physics*, *122*(7), 7834–7848. https://doi.org/10.1002/2017JA024314

Taguchi, M., Ejiri, M., & Tomimatsu, K. (2004). A new all-sky optics for aurora and airglow imaging. *Advances in Polar Upper Atmosphere Research*, *18*, 140–148.

Tsuda, T. T., Li, C., Hamada, S., Hosokawa, K., Oyama, S.-I., Nozawa, S., et al. (2020). OI 630.0-nm and N2 1PG emissions in pulsating aurora events observed by an optical spectrograph at Tromsø, Norway. *Journal of Geophysical Research: Space Physics*, *125*(12), e2020JA028250. https://doi.org/10.1029/2020JA028250

Turunen, E., Kero, A., Verronen, P. T., Miyoshi, Y., Oyama, S.-I., & Saito, S. (2016). Mesospheric ozone destruction by high-energy electron precipitation associated with pulsating aurora. *Journal of Geophysical Research: Atmospheres*, *121*(19), 11852–11861. https://doi.org/10.1002/2016JD025015

Yamamoto, T. (1988). On the temporal fluctuations of pulsating auroral luminosity. *Journal of Geophysical Research*, *93*(A2), 897–911. https://doi.org/10.1029/JA093iA02p00897